

## Swirling against the forcing: Evidence of stable counterdirected sloshing waves in orbital-shaken reservoirs

Alice Marcotte, François Gallaire , and Alessandro Bongarzone \*

*Laboratory of Fluid Mechanics and Instabilities, École Polytechnique Fédérale de Lausanne, Lausanne, CH-1015, Switzerland*



(Received 2 March 2023; accepted 7 August 2023; published 21 August 2023)

We investigate the response of the free liquid surface in a partially filled circular cylindrical container undergoing a planar elliptic and time-periodic orbit while maintaining fixed its orientation. For small forcing amplitudes and deep liquid layers, we quantify the effect of the orbit's aspect ratio on the surface dynamics in the vicinity of the fluid system's lowest natural frequency  $\omega_0$ . We provide experimental evidence of the existence of a frequency range where stable swirling can be either co- or counterdirected with respect to the container's direction of motion. Our findings are then rationalized by an inviscid weakly nonlinear model, amended with heuristic damping.

DOI: [10.1103/PhysRevFluids.8.084802](https://doi.org/10.1103/PhysRevFluids.8.084802)

### I. INTRODUCTION

The problem of liquid sloshing, i.e., the oscillations of a free liquid surface in partially filled containers, pertains to many aspects of daily life, ranging from mundane wine tasting to more pragmatic issues such as liquid spilling [1] and transport safety [2,3]. Therefore, a proper predictive understanding and modeling of the sloshing hydrodynamics at stake is essential in the design process of liquid tanks.

In this regard, the case of orbital sloshing in partially filled circular cylinders represents an archetypal sloshing system [4]. Previous experimental studies have described its resonance dynamics for circular or purely longitudinal shaking, casting light on a variety of wave regimes attracting the interest of dynamicists over the last decades [5–8].

For circular orbits, the system responds with a swirling wave codirected with the container motion [9]. This well-defined hydrodynamics, often modeled by a one-degree-of-freedom Duffing oscillator [6,10], is advantageously exploited in the design of bioreactors, where the container is shaken so as to gently mix the liquid, prevent sedimentation and enhance gas transfer [11]. In the case of longitudinal forcing, the standing wave solution may undergo a resonant symmetry breaking, with clockwise and anticlockwise swirling waves equally probable, or completely lose regularity showing an alternation of planar and swirling motions [5,12]. Such a configuration finds a close mechanical analogy in the resonant motion of a forced spherical pendulum [8], a four degrees-of-freedom system that has been widely studied in the context of order-to-chaos transitions [7,13] for its similarities with the Lorentz's problem [14].

Surprisingly, however, no experimental studies devoted to the more generic case of elliptic orbits have been reported so far in the sloshing literature. Yet, existing theoretical analyses of this forcing condition brought out interesting features of the resonant liquid response that depend on the orbit's ellipticity. In particular, the inviscid theory of Faltinsen *et al.* [15] suggests the counterintuitive existence, under resonant elliptic forcing, of stable swirling waves that propagate in the direction

---

\*alessandro.bongarzone@epfl.ch

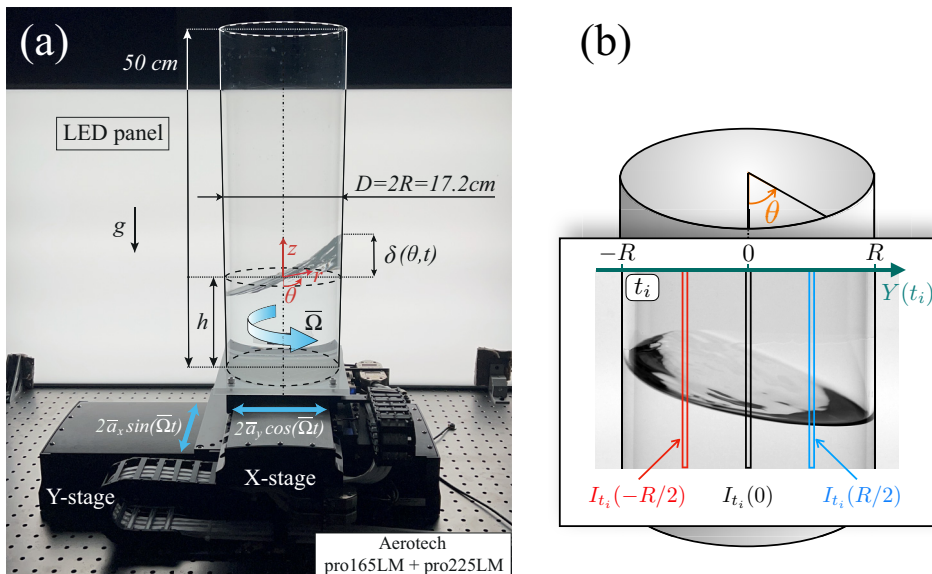


FIG. 1. (a) Experimental setup. Sloshing waves are generated by the container elliptic trajectory, achieved by imposing along the  $x$  and  $y$  axes two sinusoidal forcing of driving angular frequency  $\bar{\Omega}$  and amplitudes  $\bar{a}_x$  and  $\bar{a}_y$ .  $\delta(\theta, t)$  denotes the free surface elevation measured at the sidewall,  $r = R$ . (b) Sketch illustrating the extraction from the frame corresponding to time instant  $t_i$  of the intensity profiles along the vertical middle axis of the container image (labeled as  $I_i(0)$ ) and along the vertical axes located at coordinates  $\mp R/2$ .

opposite to the forcing direction. The theory further predicts that counterwaves may exist even for quasicircular orbits and travel with a smaller amplitude than codirected waves. However, these predictions have not been confirmed yet by experimental evidence.

For moderately large-size containers, the use of inviscid hydrodynamic models is well accepted [3]. Still, in real sloshing problems, waves are always subjected to a nonvanishing viscous dissipation. Hence, the counterswirling wave predicted by inviscid theories [15], being intrinsically disfavored by the forcing direction, is likely more sensitive to damping than coswirling solutions, and it is currently unclear whether such a solution can arise in a laboratory experiment.

With this paper, we aim to provide a joint experimental and theoretical characterisation of the free liquid surface response for a generic, elliptic periodic container trajectory so as to bridge the gap between the two diametrically opposed shaking conditions previously discussed. Specifically, we intend to identify the experimental range of external control parameters, i.e., driving frequency, amplitude, and orbit aspect ratio, for which stable counterdirected swirling waves occur and assess the extent of the forcing regime where asymptotic inviscid theoretical models break down.

The paper is organized as follows. The experimental setup and procedure are described in Sec. II. The inviscid asymptotic model, based on a weakly nonlinear multiple time scales analysis, is described in Sec. III. Section IV is dedicated to the comparisons between theory and experiments. Final conclusions are outlined in Sec. V.

## II. EXPERIMENTAL SETUP AND PROCEDURE

In our experimental campaign, we used a plexiglas circular cylindrical container of total height 50 cm and internal radius  $R = 0.086$  m, filled to a depth  $h = 0.15$  m with water: density  $\rho = 1000$  kg m $^{-3}$ , surface tension  $\gamma = 0.0725$  Nm $^{-1}$  and dynamic viscosity  $\mu = 0.001$  kg m $^{-1}$  s $^{-1}$ . The gravity acceleration is denoted by  $g$  [see Fig. 1(a)]. The container is fixed on a double-axes linear motion actuator (Aerotech pro165LM + pro225LM), which imposes along the  $x$  and  $y$  axes two

sinusoidal forcings of angular frequency  $\bar{\Omega}$  and amplitudes  $\bar{a}_x$  and  $\bar{a}_y$ , that are  $\pi/2$ -phase shifted with respect to each other. The fluid motion is recorded with a digital camera (Nikon D850) coupled with a Nikon 60mm f/2.8D lens and operated in slow mode with an acquisition frequency of 120fps. The camera's optical axis is aligned with the  $x$  axis. A LED panel is placed behind the container so as to provide a back illumination for better optical contrast.

In the moving reference frame, any planar ellipticlike shaking can be represented by the following equations describing the motion acceleration of the container axis parametrized in polar coordinates  $(r, \theta)$ ,

$$\frac{d^2 \mathbf{X}_0}{dt^2} = \begin{cases} (-f_x \cos \Omega t \cos \theta - f_y \sin \Omega t \sin \theta) \mathbf{e}_r, \\ (f_x \cos \Omega t \sin \theta - f_y \sin \Omega t \cos \theta) \mathbf{e}_\theta, \end{cases} \quad (1)$$

where  $f_x = f = \bar{a}_x \Omega^2 / R$  and  $f_y = \alpha f = \bar{a}_y \Omega^2 / R$  are the nondimensional major- and minor-axis driving acceleration components, respectively, and  $\Omega = \bar{\Omega} / \sqrt{g/R}$  the nondimensional driving angular frequency. The bar symbol refers to the dimensional quantities. Note that the minor-to-major-axis component ratio,  $\alpha = \bar{a}_y / \bar{a}_x = f_y / f_x$ , has been introduced. A value  $0 < \alpha < 1$  refers to elliptic orbits, whereas the two limiting cases  $\alpha = 0$  and  $\alpha = 1$  correspond, respectively, to longitudinal and circular shaking conditions.

With this experimental campaign we intend to study the free surface response in the vicinity of the lowest natural frequency  $\omega_0 = \bar{\omega}_0 / \sqrt{g/R} = \sqrt{k \tanh(kh/R)} = 1.3547$  (with wave number  $k = 1.8412$ ) [16], for varying orbit's aspect ratios  $\alpha$  and forcing amplitudes  $\bar{a}_x$ . In particular, we aim at recovering the whole set of stationary wave amplitude solutions, i.e., co- and counterswirling waves, and at studying how their stability depends on the forcing parameters. If coswirling and counterswirling waves happen to be coexisting stable solutions for a certain combination of control parameters, then a codirected swirling motion will very likely be naturally favored by the forcing direction and will therefore spontaneously arise from the time-harmonic forcing. On the other hand, triggering counterswirling would require escaping the basin of attraction of the coswirling wave solution, which is only possible by introducing a sufficient flow perturbation. The experimental procedure described in the following is thus suitably designed so as to reveal steady-state counter-directed waves, whenever this dynamics is a stable admissible solution.

In a typical experiment, the amplitude  $\bar{a}_x \in [1, 3]$  mm and ellipticity  $\alpha \in [0.1, 0.95]$  are fixed, while frequencies are swept upward and downward within the (dimensionless) range  $\Omega / \omega_0 \in [0.82, 1.21]$ . The increment between two consecutive steps in the frequency sweep is 0.0217. Each frequency step consists of two parts: the container undergoes first a harmonic elliptic forcing that is in the anticlockwise direction for 150 oscillation periods and then in the clockwise direction for another 150 oscillation periods. Two movies are then recorded at each step so as to monitor the free surface response to both clockwise and anticlockwise forcing. Switching the direction of the tank's trajectory in the second phase of the experimental procedure induces a flow perturbation that is enough to produce a counterdirected wave if the latter is an admissible stable configuration for the system. For each frequency step and container direction, the camera is triggered only after 100 cycles so that it only records the last 50 oscillation periods. Preliminary longer measurements performed for a few forcing parameters sampled within our experimental range showed that the transient regime typically lasts less than 100 cycles. Successively, we made sure that every movie recorded after 100 oscillation periods indeed corresponds to stationary wave amplitude regimes, except when the system exhibits the irregular dynamics described later in the section.

### A. Analysis of the free-surface response

The procedure to analyze the free surface response is extensively described in Marcotte *et al.* [17] and illustrated here in Fig. 1(b). Briefly, we build from each movie an image  $I(y) = [I_{t_1}(y), I_{t_2}(y), \dots]$  where  $I_{t_i}(y)$  is the intensity profile along the vertical axis  $Y(t_i) = y$  on the frame  $i$  corresponding to time  $t_i$ , with  $Y(t_i) = 0$  being the vertical middle axis between the edges of the container image [represented by  $Y(t_i) = R$  and  $Y(t_i) = -R$ ]. The resulting image, as illustrated in Fig. 2, displays

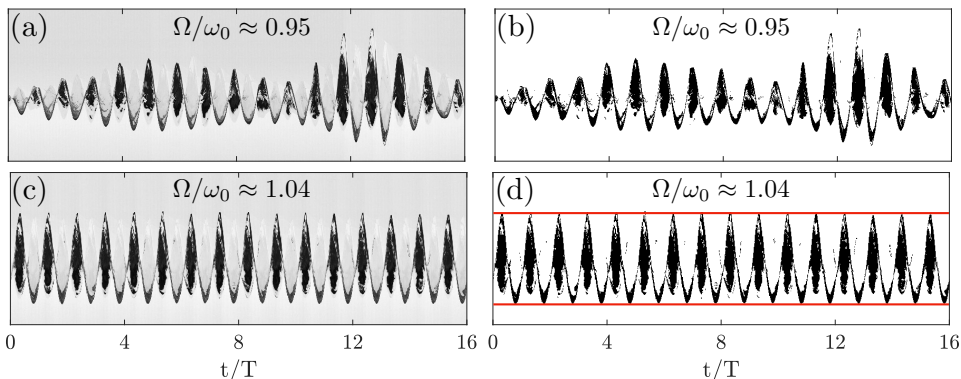


FIG. 2. (a)–(d) Intensity profiles as a function of time along the middle vertical axis  $I(0)$  for ellipticity  $\alpha = 0.5$ , amplitude  $\bar{a}_x = 1.5$  mm and frequency (a)–(b)  $\Omega/\omega_0 \approx 0.95$  or (c)–(d)  $\Omega/\omega_0 \approx 1.04$ . The intensity profiles (b) and (d) are obtained from the binarization of (a) and (c) so as to filter out the signal of weaker intensity coming from the back contact line whenever the elevation of the front contact line is minimal. The oscillations of the front contact line are then enclosed into a top-bottom envelope, plotted in red in (d).

a periodic dark pattern that represents the free surface response to the harmonic forcing. The free surface appears as the darkest feature on each frame so that the intensity profile along a vertical line at a given time  $t_i$  represents the vertical extension of the free surface in this direction.

The usefulness of the resulting image  $I(y)$  is threefold: (i) it allows the detection of irregular dynamics. This corresponds to the absence of any stable wave amplitude for a given set of forcing parameters and is easily identified by the time-varying envelope modulating the free surface oscillations, see Fig. 2(a). (ii) For a regular response,  $I(0)$  enables one to measure the amplitude of the front contact line in the azimuthal direction  $\theta = 0$ . (iii) The comparison of the profiles along two vertical directions that are mirror symmetric with respect to the vertical middle axis, e.g.,  $I(-R/2)$  and  $I(R/2)$ , makes it possible to determine the propagation direction of the wave and to compare it with the container's motion direction.

### B. Detecting the irregular regime

Figure 2 displays two intensity profiles as a function of time along the vertical middle axis ( $Y = 0$ ) for the same forcing amplitude  $\bar{a}_x$  and ellipticity  $\alpha$  but for two different forcing frequencies  $\Omega/\omega_0$ . Those images show that depending on the forcing parameters, the amplitude of the free surface oscillations can be either irregular, Figs. 2(a)–2(b), or stationary, Figs. 2(c)–2(d). In the analysis of the close-to-resonance dynamics, we, therefore, use the profile  $I(0)$  to identify the irregular regime.

### C. Measuring the wave amplitude

The intensity profile  $I(0)$  also provides the amplitude  $\delta(\theta = 0, t)$  of the swirling wave at the front wall of the container, i.e., at the azimuthal coordinate  $\theta = 0$ , such as defined in Fig. 1(b). Indeed, due to the back lighting, the intensity signal corresponding to the front contact line appears darker than the one due to the back contact line, so that pieces of information associated with the latter can be filtered out by a proper thresholding of profile  $I(0)$ . On the resulting binarized image, the maximal and minimal heights of the final periodic pattern correspond then to the peaks and troughs of the swirling wave at the front wall along  $\theta = 0$ . The amplitude of the wave (in pixel) is thus experimentally retrieved as half the difference between the height of the top and of the bottom envelopes enclosing its oscillations, displayed in Fig. 2(d) as red lines, and converted into millimeters by using a scale put on the front wall of the container. Note that in this procedure, we neglect the variation of the pixel size that can occur along the container motion, the camera being

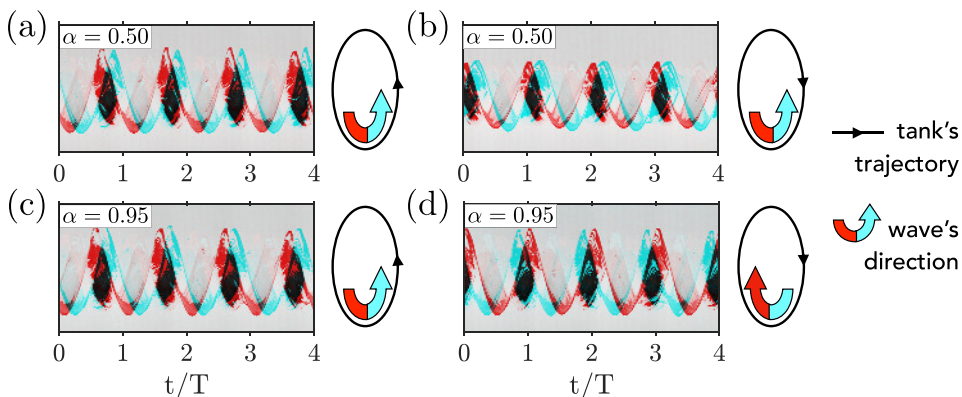


FIG. 3. Superposition of the intensity profiles as a function of time along the vertical axis ( $Y = R/2$  and  $Y = -R/2$ ), denoted  $I(R/2)$  (in blue) and  $I(-R/2)$  (in red), respectively, for a harmonic forcing of frequency  $\Omega/\omega_0 \approx 1.04$ , amplitude  $\bar{a}_x = 1.5$  mm, and (a)–(b) ellipticity  $\alpha = 0.50$  and (c)–(d)  $\alpha = 0.95$ . The container moves either in the anticlockwise direction [(a) and (c)] or in the clockwise direction [(b) and (d)]. See also movies in Supplemental Material [18].

fixed. This is justified by the very small forcing amplitude ( $1 \text{ mm} \leq \bar{a}_x \leq 3 \text{ mm}$ ) with respect to the distance between the camera and the front wall of the container (1 m). The error related to the variation of the pixel size is therefore of the order of 0.1%, i.e., negligible compared to the typical dispersion of our measurements.

#### D. Identifying the swirling direction

To detect the direction of propagation of the wave, we compare for each movie [18] the intensity profiles along two vertical directions that are mirror symmetric with respect to the vertical middle axis of the container. Figure 3 shows composite images that each consists of the superposition of  $I(R/2)$  and  $I(-R/2)$  into a composite RGB image, where gray areas correspond to pixels where  $I(R/2)$  and  $I(-R/2)$  have the same intensity, while red (blue) areas correspond to the part of  $I(-R/2)$  [ $I(R/2)$ ] that do not overlap with  $I(R/2)$  ( $I(-R/2)$ ). Thus, a red (blue) peak preceding a blue (red) peak corresponds to a wave traveling from the left (right) to the right-hand (left-hand) side of the front wall of the container, i.e., in the anticlockwise (clockwise) direction. The propagation direction of the wave can then be determined and compared to the direction of the container motion. In Fig. 3, the dynamics associated with two different aspect ratio  $\alpha = 0.5$  and  $\alpha = 0.95$  (quasicircular orbit) are compared for the same forcing frequency and amplitude. For each  $\alpha$ , the right- and left-hand side signals  $I(R/2)$  and  $I(-R/2)$  are superposed to each other for two motion configurations, namely an anti-clockwise followed by a clockwise container trajectory. In the case of the anticlockwise tank's motion, Figs. 3(a)–3(b), the swirling wave travels in the same direction as the container, but the change of container's motion direction induces a flow perturbation sufficient to produce a robust counterdirected wave, if the latter corresponds to a system's stable solution. We indeed observe in the case of  $\alpha = 0.5$  that the wave, though of smaller amplitude, is still traveling from the left- to the right-hand side of the container's front wall despite the reverse of direction in the tank trajectory. This appears glaringly in Fig. 4, where the two series of free surface snapshots show how the wave's direction of rotation remains unchanged despite the reversal of the container's direction of motion. On the contrary, Figs. 3(c)–3(d), the wave switches direction for the large ellipticity  $\alpha = 0.95$  and is therefore codirected with the forcing for both container motion directions. These results provide the first experimental evidence for the existence of counterswirling solutions and validate this procedure as suitable to trigger and identify stable counterdirected waves.

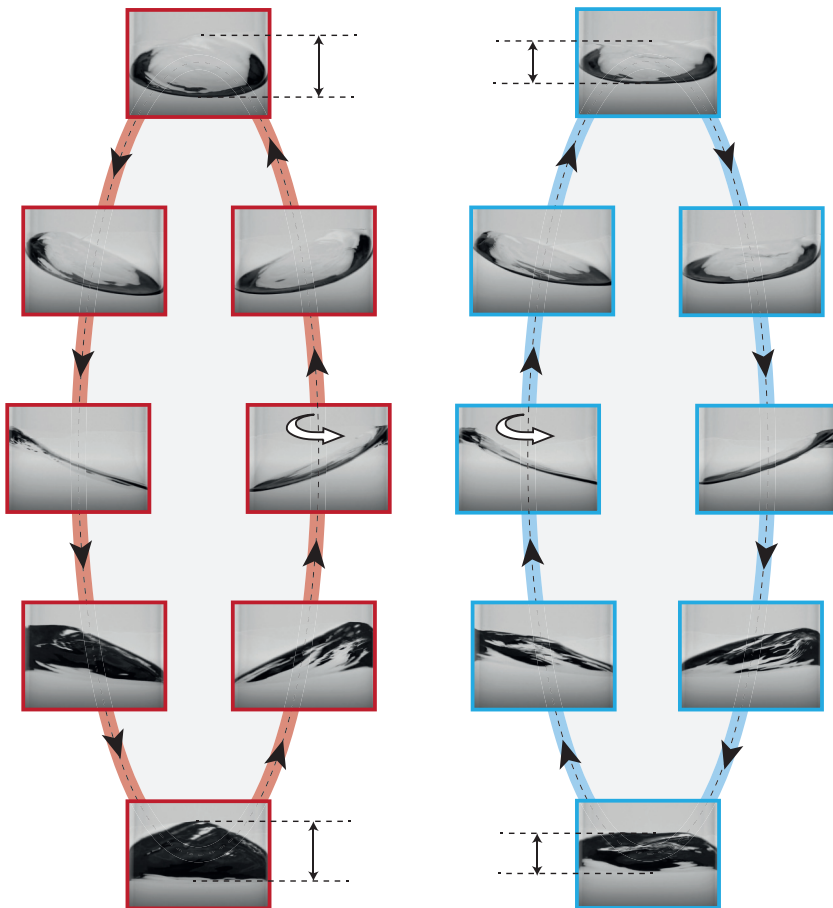


FIG. 4. Free surface snapshots corresponding to the case of Figs. 3(a)–3(b) with  $\alpha = 0.50$ . Direction of the container motion: left, anticlockwise; right, clockwise (follow the black arrows). The white arrows indicate the direction of the wave rotation. A visual indication of the different wave amplitudes is provided by the black double-sided arrows.

### III. INVISCID ASYMPTOTIC MODEL

To assess the extent of the validity of an inviscid hydrodynamic model to predict resonant counterswirling in a laboratory-scale experiment, in this section we compare our experimental results with the theoretical estimates provided by the asymptotic model formalized in Marcotte *et al.* [17] and recalled in the following. This weakly nonlinear model has been extensively compared with Faltinsen *et al.* [15] for both purely longitudinal [17] and circular [10] shaking conditions and it has been shown to provide consistent results. See Ref. [17] for a discussion on the methodological analogies and differences as well as on the pros and cons of the present approach versus the Narimanov-Moiseev multimodal theory employed in Ref. [15].

#### A. Governing equations

In the potential flow limit, i.e., the flow is assumed inviscid, irrotational and incompressible, the liquid motion is governed by the Laplace equation, subjected to the homogeneous no-penetration

condition at the solid lateral wall,  $r = R$ , and bottom  $z = -h$ ,

$$\Delta\Phi = 0, \quad \nabla\Phi \cdot \mathbf{n} = \mathbf{0}, \quad (2)$$

and by the kinematic and dynamic boundary conditions at the free surface  $z = \eta(r, \theta, t)$  [2,3],

$$\frac{\partial\eta}{\partial t} + \nabla\Phi \cdot \nabla\eta - \frac{\partial\Phi}{\partial z} = 0. \quad (3a)$$

$$\frac{\partial\Phi}{\partial t} + \frac{1}{2}\nabla\Phi \cdot \nabla\Phi + \eta = r[f_x \cos(\Omega t) \cos\theta + f_y \sin(\Omega t) \sin\theta], \quad (3b)$$

made nondimensional using the characteristic length  $R$  and velocity  $\sqrt{gR}$ .  $\Phi(r, \theta, z, t)$  and  $\eta(r, \theta, t)$  denote potential velocity field and free surface elevation, respectively. Note that, as in Ref. [15] and Ref. [17], surface tension effects have been neglected. By recalling the definition of the orbit aspect ratio,  $\alpha = \bar{a}_y/\bar{a}_x = f_y/f_x$ , so that  $f_x = f$  and  $f_y = \alpha f$ , equation (3b) can be conveniently rewritten as

$$\frac{\partial\Phi}{\partial t} + \frac{1}{2}\nabla\Phi \cdot \nabla\Phi + \eta = r\frac{f}{2}(\alpha_A e^{i(\Omega t - \theta)} + \alpha_B e^{i(\Omega t + \theta)}) + c.c., \quad (4)$$

with *c.c.* denoting the complex conjugate and with  $\alpha_A = (1 + \alpha)/2$  and  $\alpha_B = (1 - \alpha)/2$  two auxiliary orbit parameter.

### B. Multiple time scales weakly nonlinear analysis

The weakly nonlinear multiple timescale analysis formalized in Sec. IV of Marcotte *et al.* [17] is based on the following asymptotic expansion for the flow quantities,

$$\mathbf{q}(r, \theta, z, t) = \{\Phi, \eta\}^T = \mathbf{q}_0 + \epsilon\mathbf{q}_1 + \epsilon^2\mathbf{q}_2 + \epsilon^3\mathbf{q}_3 + \mathcal{O}(\epsilon^4), \quad (5)$$

and on the assumption of a small forcing amplitude of order  $f = \epsilon^3 F$ , which is justified by the fact that close to the resonance  $\Omega \approx \omega_0$ , even a small forcing will induce a large system response. We then allow for a small frequency detuning with respect to the first system's natural frequency,  $\omega_0$ , such that  $\Omega = \omega_0 + \lambda$ , with  $\lambda = \epsilon^2 \Lambda$ ,  $\epsilon$  a small parameter  $\ll 1$  and the new auxiliary parameters  $F$  and  $\Lambda$  assumed of order  $\mathcal{O}(1)$ . Note that the  $\epsilon^0$ -order solution,  $\mathbf{q}_0$  represents the rest state, for which  $\Phi_0$  and  $\eta_0$  are simply zero.

Given the azimuthal periodicity of the forcing term on the right-hand side of (4), i.e.,  $m = \pm 1$  (with  $m$  a so-called azimuthal wave number), we postulate a leading-order solution as the sum of two counterpropagating traveling waves

$$\mathbf{q}_1(r, \theta, z, t) = A_1(T_2)\hat{\mathbf{q}}_1^{A_1}(r, z)e^{i(\omega_0 t - \theta)} + B_1(T_2)\hat{\mathbf{q}}_1^{B_1}(r, z)e^{i(\omega_0 t + \theta)} + c.c. \quad (6)$$

with *c.c.* denoting the complex conjugate. As typical of multiple timescale analyses [19,20], the complex amplitudes  $A_1$  and  $B_1$ , functions of the slow time scale  $T_2 = \epsilon^2 t$  and still undetermined at this stage of the expansion, describe the slow time amplitude modulation of the two oscillating waves and must be determined at a higher order of the asymptotic expansion.

The natural frequency  $\omega_0$  and structure  $\hat{\mathbf{q}}_1^{A_1}$  (and  $\hat{\mathbf{q}}_1^{B_1}$ ) assume the meaning of eigenvalue and associated eigenmode of the leading-order linearized sloshing operator, whose matrix compact form can be written as  $(i\omega_0\mathcal{B} - \mathcal{A}_{m=\pm 1})\hat{\mathbf{q}}_1^{A_1, B_1} = 0$  (see Refs. [21], [10], and [17] for the expression of  $\mathcal{B}$  and  $\mathcal{A}_m$ ). As in Ref. [10], those matrices are numerically discretized in space by means of a Gauss-Lobatto-Chebyshev pseudospectral collocation method with a two-dimensional mapping implemented in MATLAB, which is analogous to the method described in Refs. [21] and [22].

By pursuing the expansion to the second order in  $\epsilon$ , one obtains a linear system forced by second-order nonlinear terms produced by combinations of the two leading-order waves through, e.g.,  $\nabla\Phi_1 \cdot \nabla\Phi_1/2$  in the dynamic condition and  $\nabla\Phi_1 \cdot \nabla\eta_1$  in the kinematic equation. These forcing terms,  $\hat{\mathcal{F}}_2^j$ , are proportional to  $A_1^2$  and  $B_1^2$  (second harmonics), to  $|A_1|^2$  and  $|B_1|^2$  (steady

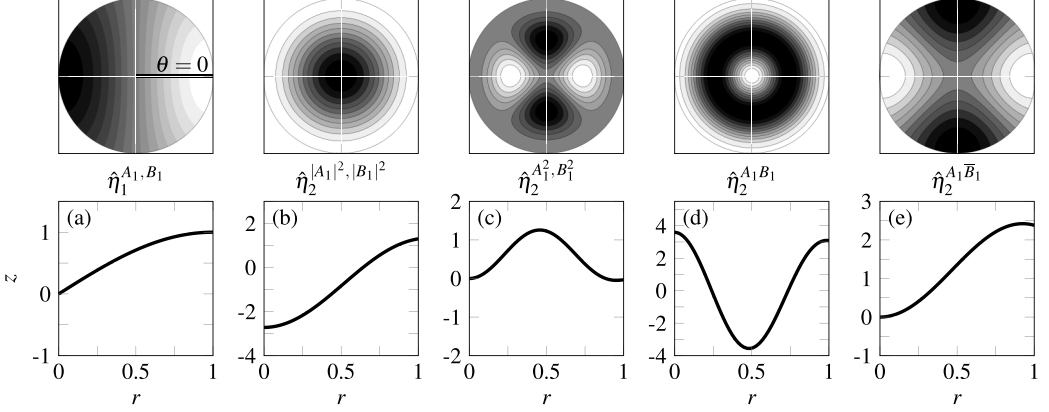


FIG. 5. (a) First-order and (b)–(e) second-order free surface deformations. Top: top-view of the full surface deformations, reconstructed according to the corresponding azimuthal periodicity and shown for  $t = 0$ , i.e.,  $\hat{\eta}_1^{A_1, B_1}(r) \cos m\theta$ . Bottom: interface as a function of the radial coordinate only and at  $\theta = 0$ , e.g.,  $\hat{\eta}_1^{A_1, B_1}(r)$ . The first-order solution is normalized with the amplitude and phase of the contact line elevation (at  $r = 1$ ), such that the free surface  $\eta_1^{A_1, B_1}$  is purely real, whereas the potential velocity field  $\Phi_1^{A_1, B_1}$  is purely imaginary. Note that, owing to the symmetries of the problem, the system admits the following invariant transformation:  $(\hat{\mathbf{q}}, +m, i\omega_0) \rightarrow (\hat{\mathbf{q}}, -m, i\omega_0)$ , so that  $\hat{\eta}_1^{A_1} = \hat{\eta}_1^{B_1}$ ,  $\hat{\eta}_2^{A_1|^2} = \hat{\eta}_2^{B_1|^2}$  and  $\hat{\eta}_2^{A_1^2} = \hat{\eta}_2^{B_1^2}$ . In other words, only part of the first and second-order responses need to be computed explicitly.

and axisymmetric mean flow corrections) and to  $A_1 B_1$  and  $A_1 \bar{B}_1$  (cross-quadratic interactions), and therefore they call for a second-order solution in the form

$$\mathbf{q}_2 = |A_1|^2 \hat{\mathbf{q}}_2^{A_1 \bar{A}_1} + |B_1|^2 \hat{\mathbf{q}}_2^{B_1 \bar{B}_1} + (A_1^2 \hat{\mathbf{q}}_2^{A_1 A_1} e^{i2(\omega_0 t - \theta)} + B_1^2 \hat{\mathbf{q}}_2^{B_1 B_1} e^{i2(\omega_0 t + \theta)} + \text{c.c.}) \\ + (A_1 B_1 \hat{\mathbf{q}}_2^{A_1 B_1} e^{i2\omega_0 t} + A_1 \bar{B}_1 \hat{\mathbf{q}}_2^{A_1 \bar{B}_1} e^{-i2\theta} + \text{c.c.}). \quad (7)$$

None of the associated forcing terms being resonant, each spatial structure,  $\hat{\mathbf{q}}_2^{ij}(r, z)$  can be computed numerically as described in Ref. [10] by simply inverting the corresponding linear operator, e.g.,

$$\hat{\mathbf{q}}_2^{A_1 \bar{A}_1} = (-\mathcal{A}_0)^{-1} \hat{\mathcal{F}}_2^{A_1 \bar{A}_1}, \quad \hat{\mathbf{q}}_2^{A_1 A_1} = (i2\omega_0 \mathcal{B} - \mathcal{A}_{-2})^{-1} \hat{\mathcal{F}}_2^{A_1 A_1}, \\ \hat{\mathbf{q}}_2^{A_1 B_1} = (i2\omega_0 - \mathcal{A}_0)^{-1} \hat{\mathcal{F}}_2^{A_1 B_1}, \quad \hat{\mathbf{q}}_2^{A_1 \bar{B}_1} = (-\mathcal{A}_{-2})^{-1} \hat{\mathcal{F}}_2^{A_1 \bar{B}_1}. \quad (8)$$

The resulting structures are shown in Fig. 5 in terms of free surface deformations.

We now move forward to the  $\epsilon^3$ -order problem, which is once again a linear problem forced by combinations of the first- (6) and second-order (7) solutions, produced by third-order nonlinearities through, e.g.,  $(\nabla \Phi_1 \cdot \nabla \Phi_2 + \nabla \Phi_2 \cdot \nabla \Phi_1)/2$  in the dynamic condition or  $\nabla \Phi_1 \cdot \nabla \eta_2 + \nabla \Phi_2 \cdot \nabla \eta_1$  in the kinematic equation, as well as by the slow time- $T_2$  derivative of the leading-order solution and by the external forcing, which was assumed of order  $\epsilon^3$ :

$$(\partial_t \mathcal{B} - \mathcal{A}_m) \mathbf{q}_3 = \mathcal{F}_3 = -\frac{\partial A_1}{\partial T_2} \mathbf{B} \hat{\mathbf{q}}_1^{A_1} e^{i(\omega_0 t - \theta)} - \frac{\partial B_1}{\partial T_2} \mathbf{B} \hat{\mathbf{q}}_1^{B_1} e^{i(\omega_0 t + \theta)} \\ + |A_1|^2 A_1 \hat{\mathcal{F}}_3^{|A_1|^2 A_1} e^{i(\omega_0 t - \theta)} + |B_1|^2 B_1 \hat{\mathcal{F}}_3^{|B_1|^2 B_1} e^{i(\omega_0 t + \theta)} \\ + |B_1|^2 A_1 \hat{\mathcal{F}}_3^{|B_1|^2 A_1} e^{i(\omega_0 t - \theta)} + |A_1|^2 B_1 \hat{\mathcal{F}}_3^{|A_1|^2 B_1} e^{i(\omega_0 t + \theta)} \\ + \alpha_a F \hat{\mathcal{F}}_3^F e^{i(\omega_0 t - \theta)} e^{i\Lambda T_2} + \alpha_b F \hat{\mathcal{F}}_3^F e^{i(\omega_0 t + \theta)} e^{i\Lambda T_2} \\ + \text{N.R.T.} + \text{c.c.}, \quad (9)$$



with  $\hat{\mathcal{F}}_3^F = \{0, r/2\}^T$  and where N.R.T. stands for nonresonating terms. The latter terms are not strictly relevant for further analysis and can therefore be neglected. The arbitrariness on amplitudes  $A_1$  and  $B_1$  is fixed by requiring that secular terms do not appear in the solution to Eq. (9), where secularity results from all resonant forcing terms in  $\mathcal{F}_3$  (see Appendix D of Ref. [10] for its explicit expression), i.e., all terms sharing the same frequency and wave number of  $\mathbf{q}_1$ , e.g.,  $(\omega_0, m = \pm 1)$ , and in effect, all terms explicitly written in (9). It follows that a compatibility condition must be enforced through the Fredholm alternative [23], which imposes the amplitudes  $A = \epsilon A_1 e^{-i\lambda t}$  and  $B = \epsilon B_1 e^{-i\lambda t}$  to obey the following normal form:

$$\frac{dA}{dt} = -i\lambda A + i\alpha_a \mu f + i\nu |A|^2 A + i\xi |B|^2 A, \quad (10a)$$

$$\frac{dB}{dt} = -i\lambda B + i\alpha_b \mu f + i\nu |B|^2 B + i\xi |A|^2 B, \quad (10b)$$

where the physical time  $t = T_2/\epsilon^2$  has been reintroduced and where forcing amplitude and detuning parameter are recast in terms of their corresponding physical values,  $f = \epsilon^3 F$  and  $\lambda = \epsilon^2 \Lambda = \Omega - \omega_0$ , so as to eliminate the small implicit parameter  $\epsilon$  [24,25].

The values of the normal form coefficients  $\mu$ ,  $\nu$ , and  $\xi$  as a function of the nondimensional fluid depth,  $H = h/R$ , are reported in Appendix A. These coefficients, which turn out to be real-valued quantities due to the absence of dissipation, are computed as scalar products between the adjoint mode,  $(\hat{\mathbf{q}}_1^{A_1^\dagger}, \hat{\mathbf{q}}_1^{B_1^\dagger})$ , associated with  $(\hat{\mathbf{q}}_1^{A_1}, \hat{\mathbf{q}}_1^{B_1})$ , and the third-order resonant forcing terms:

$$i\mathcal{I}\mu = \langle \hat{\mathbf{q}}_1^{A_1^\dagger}, \hat{\mathcal{F}}_3^F \rangle = \int_0^1 (r/2) \bar{\eta}_1^{A_1^\dagger} r dr, \quad (11a)$$

$$i\mathcal{I}\nu = \langle \hat{\mathbf{q}}_1^{A_1^\dagger}, \hat{\mathcal{F}}_3^{|A_1|^2 A_1} \rangle = \int_0^1 \left( \bar{\eta}_1^{A_1^\dagger} \hat{\mathcal{F}}_{3\text{dyn}}^{|A_1|^2 A_1} + \bar{\Phi}_1^{A_1^\dagger} \hat{\mathcal{F}}_{3\text{kin}}^{|A_1|^2 A_1} \right) r dr, \quad (11b)$$

$$i\mathcal{I}\xi = \langle \hat{\mathbf{q}}_1^{A_1^\dagger}, \hat{\mathcal{F}}_3^{|B_1|^2 A_1} \rangle = \int_0^1 \left( \bar{\eta}_1^{A_1^\dagger} \hat{\mathcal{F}}_{3\text{dyn}}^{|B_1|^2 A_1} + \bar{\Phi}_1^{A_1^\dagger} \hat{\mathcal{F}}_{3\text{kin}}^{|B_1|^2 A_1} \right) r dr, \quad (11c)$$

where

$$\mathcal{I} = \langle \hat{\mathbf{q}}_1^{A_1^\dagger}, \mathbf{B}\hat{\mathbf{q}}_1^{A_1} \rangle = \int_0^1 \left( \bar{\eta}_1^{A_1^\dagger} \hat{\Phi}_1^{A_1} + \bar{\Phi}_1^{A_1^\dagger} \hat{\eta}_1^{A_1} \right) r dr. \quad (12)$$

Here  $(\hat{\mathbf{q}}_1^{A_1^\dagger}, \hat{\mathbf{q}}_1^{B_1^\dagger}) = (\bar{\hat{\mathbf{q}}}_1^{A_1}, \bar{\hat{\mathbf{q}}}_1^{B_1})$ , since the inviscid problem is self-adjoint with respect to the Hermitian scalar product  $\langle \mathbf{a}, \mathbf{b} \rangle = \int_V \bar{\mathbf{a}} \cdot \mathbf{b} dV$ , with  $\mathbf{a}$  and  $\mathbf{b}$  two generic vectors (see Ref. [26] for a thorough discussion and derivation of the adjoint problem).

For the sake of brevity, we do not report the expression of the various forcing terms. As an example, the full expression of  $\hat{\mathcal{F}}_{3\text{kin}}^{|A_1|^2 A_1}$  is given in Appendix D of Ref. [10]. The other forcing terms are calculated analogously.

### C. Phenomenological damping coefficient

Consistently with the inviscid analysis of Faltinsen *et al.* [15], the system of amplitude equations (10a)–(10b) unrealistically predicts counterwaves for  $\alpha \rightarrow 1$  [15,27], while the condition  $\alpha = 1$  gives only codirected waves [9,28] (see Appendix C for further details). This implies that the response curve branching is not a continuous function of  $\alpha$ , which is in contradiction with our experimental evidence reported in the next section. By analogy with Raynovskyy and Timokha [27], we, therefore, introduce in Eqs. (10a)–(10b) a heuristic damping coefficient,  $\sigma$ , that serves to regularize the limit for  $\alpha \rightarrow 1$ .

The value of  $\sigma$  is estimated according to the well-known expression [29–31]

$$\sigma = \underbrace{\frac{2k^2}{Re}}_{\text{bulk}} + \underbrace{\sqrt{\frac{\omega_0}{2Re}} \left( \frac{k \cosh^2 kH}{\sinh 2kH} \right)}_{\text{surf. contamination}} + \underbrace{\sqrt{\frac{\omega_0}{2Re}} \left( \frac{k}{\sinh 2kH} + \frac{1}{2} \frac{1 + (1/k)^2}{1 - (1/k)^2} - \frac{kH}{\sinh 2kH} \right)}_{\text{bottom sidewall}}. \quad (13)$$

The damping associated with lowest natural frequency,  $\omega_0 = \bar{\omega}_0/\sqrt{g/R} = \sqrt{k \tanh(kH)} = 1.3547$  (with wave number  $k = 1.8412$ ) [16], in a container of diameter  $D = 2R = 0.172$  m filled to a depth  $H = h/R = 1.744$  with distilled water, i.e.,  $\rho = 1000$  kg/m<sup>3</sup>,  $\mu = 0.001$  kg/ms and  $\gamma = 0.072$  N/m, for which  $Re = \rho\sqrt{gR^3}/\mu = 78952$  (Reynolds number), amounts to  $\sigma = 0.0055$ . Typically the viscous damping rate can be interpreted as a slow damping process [21,32], i.e.,  $1/\sigma \approx 180$ , over a faster time scale represented by the wave oscillation, i.e.,  $1/\omega_0 \approx 0.5$ . When this hypothesis holds, as in the present experimental study, the damping coefficient is assumed to be small of order  $\epsilon^2$ , such that damping terms as  $-\sigma A$  and  $-\sigma B$ , both of order  $\sim O(\epsilon^3)$  [ $A, B \sim O(\epsilon)$ ], can be phenomenologically added *a posteriori* to the final inviscid amplitude equations.

Before moving forward, it is worth noticing that expression (13) englobes different effects, i.e., viscous dissipation occurring in the Stokes boundary layers (at the solid lateral and bottom wall), bulk dissipation and possible sources of dissipation associated with free surface contamination effects [29,33], but it does not account for any form of dissipation induced by contact angle dynamics [22,34–37] or by wave breaking and overturning [27].

Moreover, as pointed out in Appendix A of Ref. [10], prediction (13) is only valid for small-amplitude capillary-gravity waves, whereas the dissipation rates of forced wave motions are generally more complex, i.e., it is typically a function of the wave amplitude [27]. A more rigorous viscous analysis would indeed produce complex eigenfunctions and, therefore, complex-valued normal form coefficients [25], e.g.,  $v = \text{Re}[v] + i \text{Im}[v]$  (same for  $\xi$ ), so that the effective damping will be asymptotically proportional to the square of the wave amplitude through the cubic term in the amplitude equation, i.e.,  $(\sigma + \text{Im}[v]|A|^2 + \text{Im}[\xi]|B|^2)$  for amplitude  $A$  and  $(\sigma + \text{Im}[v]|B|^2 + \text{Im}[\xi]|A|^2)$  for amplitude  $B$ .

For these reasons, we do not expect the heuristic damping model to provide an accurate estimation of the actual amplitude-dependent dissipation of the system, crucial for a correct prediction of the phase lag between forcing and the system response [38]. However, accounting for a damping coefficient  $\sigma$  in Eqs. (14a)–(14b) is essential in order to regularize the weakly nonlinear model prediction as the orbit aspect ratio  $\alpha$  approaches 1, e.g., for circular orbits.

#### D. Lowest-order asymptotic solution

In conclusion, after accounting for the small damping terms  $-\sigma A$  and  $-\sigma B$ , the lowest-order asymptotic solution governing the close-to-resonance interaction of the two  $m = \pm 1$  counterpropagating waves is ruled by the following system of complex amplitude equations

$$\frac{dA}{dt} = -(\sigma + i\lambda)A + i\mu\alpha_A f + i\nu|A|^2 A + i\xi|B|^2 A, \quad (14a)$$

$$\frac{dB}{dt} = -(\sigma + i\lambda)B + i\mu\alpha_B f + i\nu|B|^2 B + i\xi|A|^2 B. \quad (14b)$$

The leading-order free surface deformation writes

$$\eta(r, \theta, t) = \hat{\eta}_1^{A_1, B_1}(r) (A e^{i(\Omega t - \theta)} + B e^{i(\Omega t + \theta)}) + \text{c.c.} \quad (15)$$

Given the choice of the mode normalization, for which  $\hat{\eta}_1^{A_1, B_1}(r=1) = 1$ , we can express the dimensionless contact line elevation,  $\delta(\theta, t)/R$ , at any azimuthal coordinate, e.g., at  $\theta = 0$ , as

$$\delta(0, t)/R = (A + B)e^{i\Omega t} + \text{c.c.} \quad (16)$$

This quantity will be used in the next section for comparison with the experimental measurements of the stable stationary wave amplitudes. The stationary solutions and their stability can be computed and predicted from (14a)–(14b) as explained in Appendix B.

#### IV. COMPARISON WITH EXPERIMENTS

We now compare, in Fig. 6, our measurements to the asymptotic model (14a)–(14b). It is important to note that the comparison is outlined only in terms of steady-state wave amplitude. In other words, the experimental transient dynamics following the reverse of the container’s direction of motion is ignored and, more generally, the specific structure of such an initial perturbation does not enter the theoretical model, as we only look for large time stationary solutions of Eqs. (14a)–(14b) with  $d/dt = 0$ .

Figure 6 shows that at small ellipticity, e.g.,  $\alpha$  close to 0.10, the amplitude response curve is similar to that induced by a purely longitudinal forcing [12,17] except that the planar wave solution no longer exists, owing to the preferential direction of motion, and that the co- and counterrotating waves are no more equally probable, with the counterwave exhibiting a slightly lower amplitude. By increasing the value of  $\alpha$ , the counterwave displays a decreasing amplitude and the range of frequency for which irregular motion occurs shrinks down and ultimately vanishes [15]. For longitudinal sloshing, irregular motions are the result of an irregular alternation of planar and swirling dynamics [12]. In the context discussed here, irregular means that both the co- and counterswirling solutions are unstable and the system exhibits irregular and chaotic patterns switching between co- and, at a small ellipticity, counterswirling dynamics alternating transient intervals of nearly planar motions (see also movies in Supplemental Material [18]). As  $\alpha$  approaches 1, the admissible frequency range associated with counterwaves reduces and it is eventually suppressed, whereas the frequency range associated with codirected swirling widens and covers all of the frequency range at  $\alpha = 0.95$ , i.e., approaching the limiting case of a circular trajectory ( $\alpha = 1$ ) [9,10]. We also observe a decrease in the wave amplitude at  $\bar{a}_x = 3$  mm for  $\alpha \geq 0.5$ , occurring just before the jump-down frequency (see gray boxes in Fig. 6) and which can be tentatively attributed to highly nonlinear effects, e.g., wave breaking leading to the atomization of the wave crests, overlooked by the weakly nonlinear model.

The experimental steady-state wave amplitudes are in good quantitative agreement with the theoretical predictions for all  $\bar{a}_x$  and  $\alpha$  values explored, hence proving the validity of the inviscid analysis in our regime of operation. The only major limitation of the asymptotic analysis is intrinsic to the use of a simple phenomenological damping. As the latter does not depend on the wave amplitude, it cannot accurately predict the phase lag between forcing and the system response [38]. This translates into an imprecise estimation of the jump-down frequency occurring above resonance and of the frequency range associated with the counter-swirling, which appears slightly overestimated.

#### V. CONCLUSION

In this work, we have investigated the sloshing dynamics in the vicinity of the first harmonic resonance for container elliptic orbits. The amplitude-response curves at different forcing amplitudes were examined versus the orbit’s aspect ratio. We have reported for the first time experimental evidence of the existence of a frequency range where stable swirling can be counterdirected with respect to the container’s direction of motion. Particularly, our experiments demonstrated the existence of a significant frequency range associated with stable counterswirling up to surprisingly high orbit aspect ratios.

Our findings have been rationalized by the asymptotic model formalized in Marcotte *et al.* [17] supplemented with a heuristic damping coefficient, which shows how the close-to-resonant sloshing dynamics for any container’s ellipticlike orbit is well represented by four degrees of freedom only. This suggests that generalizing the resonantly forced spherical pendulum [7] could provide

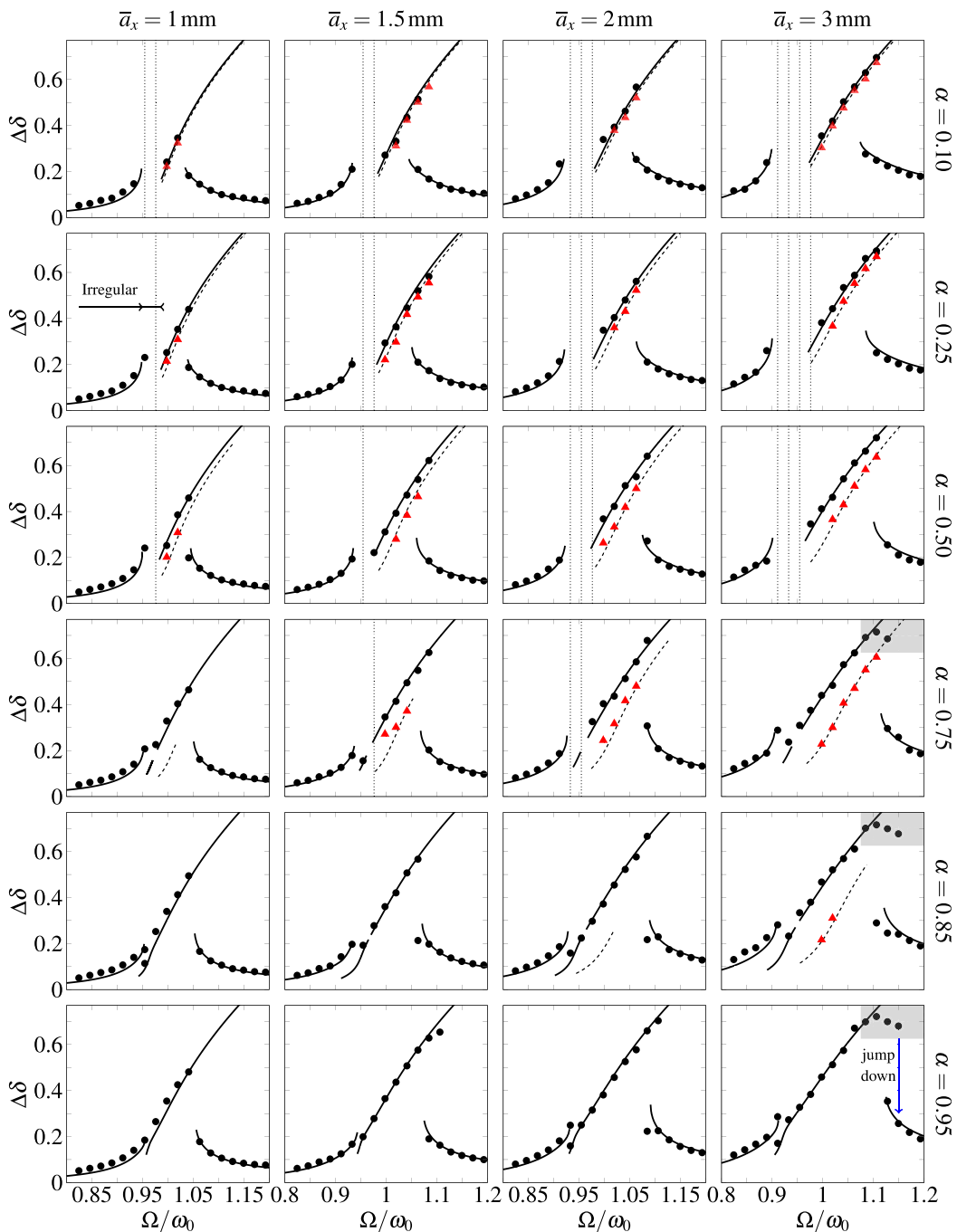


FIG. 6. Nondimensional wave amplitude,  $\Delta\delta = [\max_t \delta(0, t) - \min_t \delta(0, t)]/2R$  versus  $\Omega/\omega_0$  for different values of  $\bar{a}_x$  (rows) and  $\alpha$  (columns). Markers: experiments (black for co- and red for counterwaves). The typical dispersion in the measurements is well represented by the size of the markers. Curves: stable branches predicted by the present WNL theory (solid for co- and dashed for counterwaves). Vertical dotted lines indicate frequency values at which experiments have shown irregular motion. Unstable branches are not displayed for the sake of clarity.

TABLE I. Value of the normal form coefficients appearing in (14a)–(14b) computed at different non-dimensional fluid depths  $H = h/R$  (as reported in Table I of Marcotte *et al.* [17]) and associated with the lowest natural frequency mode. The subscript SC was used in Refs. [10] and [17] to indicate the shape of the associated free surface response close to harmonic resonance, initially denominated single-crest (SC) by Reclari *et al.* [9]. Here the subscript SC has been omitted, but in practice,  $\mu$ ,  $\nu$ , and  $\xi$  coincide with  $\mu_{SC}$ ,  $\nu_{SC}$ , and  $\xi_{SC}$  in Ref. [17]. For completeness, we also report the value of the system’s lowest natural frequency  $\omega_0$ . The bold values correspond to those used in the main document for comparison with experiments.

$H = h/R$	1.1	1.2	1.3	1.4	1.5	1.6	1.7	<b>1.744</b>	1.8	1.9	2.0
$\mu$	-0.279	-0.280	-0.281	-0.282	-0.283	-0.283	-0.283	<b>-0.283</b>	-0.284	-0.284	-0.284
$\nu$	1.414	1.407	1.406	1.407	1.409	1.410	1.411	<b>1.412</b>	1.412	1.412	1.412
$\xi$	-7.487	-7.914	-8.101	-8.211	-8.281	-8.328	-8.359	<b>-8.369</b>	-8.381	-8.395	-8.405
$\omega_0$	1.334	1.341	1.346	1.349	1.352	1.353	1.354	<b>1.355</b>	1.355	1.356	1.356

a suitable mechanical analogy for this entire family of sloshing dynamics, thus offering additional room in this archetypical low degrees-of-freedom class of dynamical systems.

We have discussed how the phenomenological damping is sufficient to resolve the singular limiting behavior for  $\alpha \rightarrow 1$ , but its simplistic estimation does not allow for an accurate prediction of the jump-down frequency and of the frequency range associated with counterswirling. The adequate embedding of dissipative viscous effects is a longstanding problem in the hydrodynamics community and still represents a current key challenge in modeling sloshing dynamics. The use of machine learning algorithms has been recently suggested as a pursuable approach [39], but their use obviously requires the *a priori* knowledge of an experimental dataset for training. Therefore, future perspectives of this work could include the extension of the weakly nonlinear model to a viscous framework in the same spirit as Bongarzone *et al.* [25]. Although the latter presently hinges on the subtle modeling of the moving contact line dynamics, such an extension is desirable, as it would enable one to better quantify the overall system dissipation and also to predict the viscous streaming experimentally observed in orbitally shaken containers [40].

## ACKNOWLEDGMENTS

We acknowledge the financial support of the Swiss National Science Foundation under Grants No. 178971 and No. 200341. The authors declare the absence of any conflict of interest.

## APPENDIX A: VALUES OF THE NORMAL FORM COEFFICIENTS

In Table I we report the values of the normal form coefficients,  $\mu$ ,  $\nu$ , and  $\xi$  appearing in (14a)–(14b) as a function of the nondimensional fluid depth  $H = h/R$ . Note that our experiments have been performed at a fluid depth  $H = 1.744$ .

For completeness we also report the value of the system’s lowest natural frequency  $\omega_0$ , which satisfies the well-known dispersion relation for gravity waves  $\omega_0 = \bar{\omega}_0/\sqrt{g/R} = \sqrt{k \tanh(kH)}$  (with  $k = 1.8412$ ) [16]. We do not report the value of the damping coefficient  $\sigma$  as a function of  $H$ , since for  $H \geq 1$  the fluid depth does not affect significantly its value estimated according to (13).

## APPENDIX B: STATIONARY WAVE AMPLITUDE SOLUTIONS AND THEIR STABILITY

By turning (14a)–(14b) into polar coordinates, i.e.,  $A = |A|e^{i\Phi_A}$  and  $B = |B|e^{i\Phi_B}$ , we can split real and imaginary parts, hence obtaining

$$\frac{d|A|}{dt} = -\sigma|A| + \alpha_A \mu f \sin \Phi_A, \quad (\text{B1a})$$

$$|A| \frac{d\Phi_A}{dt} = -\lambda|A| + \alpha_A \mu f \cos \Phi_A + \nu|A|^3 + \xi|B|^2|A|, \quad (\text{B1b})$$

$$\frac{d|B|}{dt} = -\sigma|B| + \alpha_B \mu f \sin \Phi_B, \quad (\text{B1c})$$

$$|B| \frac{d\Phi_B}{dt} = -\lambda|B| + \alpha_B \mu f \cos \Phi_B + \nu|B|^3 + \xi|A|^2|B|. \quad (\text{B1d})$$

Let us then decompose amplitudes and phases as the sum of stationary values plus time-dependent small perturbations of order  $\epsilon \ll 1$ .

$$\mathbf{y}(t) = \begin{pmatrix} |A|(t) \\ \Phi_A(t) \\ |B|(t) \\ \Phi_B(t) \end{pmatrix} = \begin{pmatrix} a_0 \\ \phi_{A,0} \\ b_0 \\ \phi_{B,0} \end{pmatrix} + \epsilon \begin{pmatrix} a_1(t) \\ \phi_{A,1}(t) \\ b_1(t) \\ \phi_{B,1}(t) \end{pmatrix} = \mathbf{y}_0 + \epsilon \mathbf{y}_1(t) = \mathbf{y}_0 + \epsilon (\hat{\mathbf{y}}_1 e^{st} + \text{c.c.}), \quad (\text{B2})$$

with  $s = s_r + is_i \in \mathbb{C}$  an eigenvalue and c.c. denoting the complex conjugate part of the small linear perturbation. The substitution of (B2) in (B1a)–(B1d) and the linearization around  $\mathbf{y}_0$ , lead to two problems at order  $\epsilon^0$  and  $\epsilon$ , respectively. As the nonlinear system of equations at order  $\epsilon^0$  does not admit an analytical solution, we apply a numerical procedure after rewriting the problem in the form:

$$\mathcal{F} = 0 = \begin{cases} \alpha_A \mu f \sin \phi_{A,0} - \sigma a_0, \\ \alpha_A \mu f \cos \phi_{A,0} - a_0 (\lambda - \nu a_0^2 - \xi b_0^2), \\ \alpha_B \mu f \sin \phi_{B,0} - \sigma b_0, \\ \alpha_B \mu f \cos \phi_{B,0} - b_0 (\lambda - \nu b_0^2 - \xi a_0^2). \end{cases} \quad (\text{B3})$$

System (B3) is then solved in MATLAB function using the built-in function *fsolve* and prescribing some initial guesses (*ig*) for  $(a_0^{ig}, \phi_{A,0}^{ig}, b_0^{ig}, \phi_{B,0}^{ig})$ . In practice, we provide in input the external control parameters,  $\Omega$ ,  $a_x = \bar{a}_x/R$  and  $\alpha$ , whereas the associated combination of stationary amplitudes and phases,  $(a_0, \phi_{A,0}, b_0, \phi_{B,0})$  are computed as outputs.

In the following we study the stability properties of these steady-state amplitude and phase solutions. Given the ansatz  $\mathbf{y}_1(t) = \hat{\mathbf{y}}_1 e^{st} + \text{c.c.}$ , at order  $\epsilon$  the linearized and unsteady system, describing the evolution of small amplitude perturbations around the stationary states can be written in a matrix form as

$$s\mathbf{M}\hat{\mathbf{y}}_1 = \mathbf{K}\hat{\mathbf{y}}_1, \quad (\text{B4})$$

with matrices  $\mathbf{M}$  and  $\mathbf{K}$  reading

$$\mathbf{M} = \begin{bmatrix} 1 & 0 & 0 & 0 \\ 0 & a_0 & 0 & 0 \\ 0 & 0 & 1 & 0 \\ 0 & 0 & 0 & b_0 \end{bmatrix}, \quad \mathbf{K} = \begin{bmatrix} K_{11} & K_{12} & 0 & 0 \\ K_{21} & K_{22} & K_{24} & 0 \\ 0 & 0 & K_{33} & K_{34} \\ K_{41} & 0 & K_{43} & K_{44} \end{bmatrix}, \quad (\text{B5})$$

$\hat{\mathbf{y}}_1 = (\hat{a}_1, \hat{\phi}_{A,1}, \hat{b}_1, \hat{\phi}_{B,1})^T$  and

$$K_{11} = -\sigma, \quad K_{33} = -\sigma, \quad (\text{B6a})$$

$$K_{12} = \alpha_A \mu f \cos \phi_{A,0}, \quad K_{34} = \alpha_B \mu f \cos \phi_{B,0}, \quad (\text{B6b})$$

$$K_{21} = -\lambda + 3\nu a_0^2 + \xi b_0^2, \quad K_{43} = -\lambda + 3\nu b_0^2 + \xi a_0^2, \quad (\text{B6c})$$

$$K_{22} = -\alpha_A \mu f \sin \phi_{A,0}, \quad K_{44} = -\alpha_B \mu f \sin \phi_{B,0}, \quad (\text{B6d})$$

$$K_{24} = 2\xi a_0 b_0, \quad K_{41} = 2\xi a_0 b_0, \quad (\text{B6e})$$

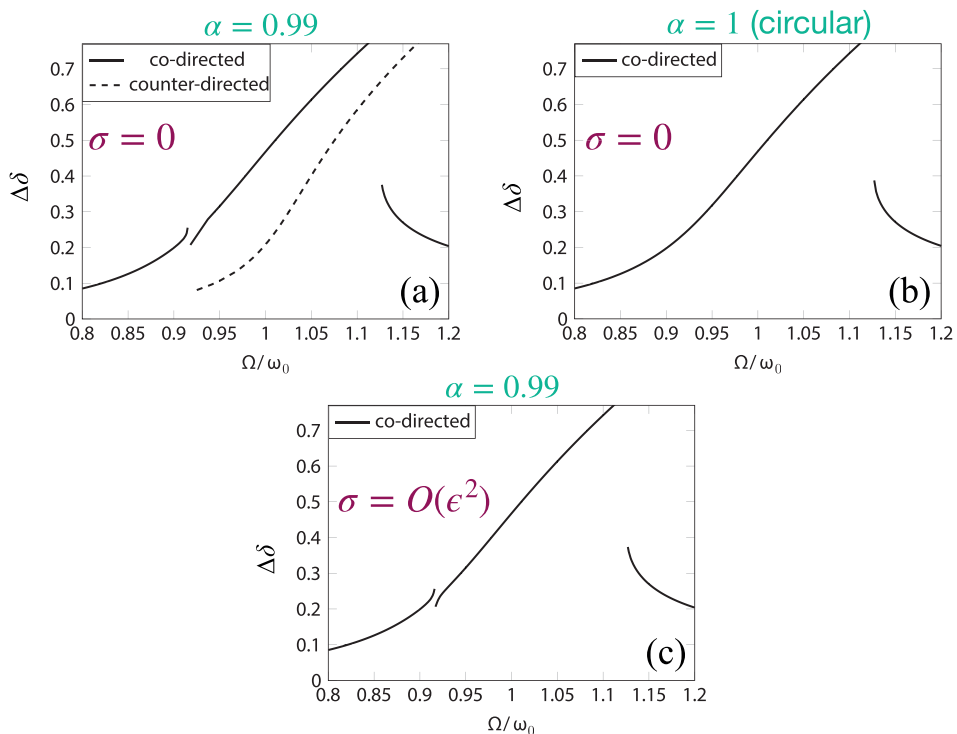


FIG. 7. Close-to-resonance branching diagram illustrated in terms of dimensionless wave amplitude,  $\Delta\delta$ , versus the rescaled forcing frequency  $\Omega/\omega_0$  and for  $\bar{a}_x = 3$  mm. (a)  $\alpha = 0.99$  and  $\sigma = 0$ ; (b)  $\alpha = 1$  and  $\sigma = 0$ ; (c)  $\alpha = 0.99$  as in (a), but  $\sigma = 0.0055$  as prescribed by Eq. (13). (c) shows how accounting for a small damping coefficient is sufficient to suppress the counterdirected swirling branch for  $\alpha = 0.99$ , hence regularizing the branching diagram in the limit of  $\alpha \rightarrow 1$  clearly highlighted by (a) and (b) for  $\sigma = 0$ .

We proceed as follows. For each  $(a_0, \phi_{A,0}, b_0, \phi_{B,0})$ , solution of (B3), we obtain four eigenvalues  $s$ . If the real part of at least one of these eigenvalues is positive, then that configuration, associated with the set of external parameters  $(\Omega, a_x, \alpha)$ , is labeled as unstable.

### APPENDIX C: BIFURCATION DIAGRAM FOR $\alpha \rightarrow 1$

In this Appendix, we illustrate the role of the phenomenological damping coefficient on the branching diagram in the limit of  $\alpha \rightarrow 1$ . Indeed, we have observed in our experiments that for increasing  $\alpha$ , the frequency range associated with the existence of a stable counterswirling wave progressively shrinks until it eventually disappears (for  $\bar{a}_x = 3$  mm, this occurs between  $\alpha = 0.85$  and  $\alpha = 0.95$ ). However, as discussed in Sec. III C, the inviscid model predicts an extended branch associated with stable counterdirected waves for any  $\alpha < 1$ , e.g.,  $\alpha = 0.99$  [see Fig. 7(a)], and no branch at all for  $\alpha$  exactly equal to 1 [Fig. 7(b)], thus indicating that the response curves branching is not a continuous function of  $\alpha$ . Instead, accounting for a damping coefficient,  $\sigma$ , allows for a continuous shrinking of the counterdirected wave branch, that eventually disappears [Fig. 7(c)], in qualitative agreement with our experimental observations.

- [1] H. C. Mayer and R. Krechetnikov, Walking with coffee: Why does it spill? *Phys. Rev. E* **85**, 046117 (2012).
- [2] O. M. Faltinsen and A. N. Timokha, *Sloshing* (Cambridge University Press, Cambridge, 2009).
- [3] R. A. Ibrahim, *Liquid Sloshing Dynamics: Theory and Applications* (Cambridge University Press, Cambridge, 2005).
- [4] H. N. Abramson, The dynamic behavior of liquids in moving containers, with applications to space vehicle technology, NASA Tech. Rep. SP-106 (NASA, Washington, 1966).
- [5] R. E. Hutton, An investigation of nonlinear, nonplanar oscillations of fluid in cylindrical container, NASA Tech. Rep. No. D-1870 (NASA, 1963).
- [6] J. R. Ockendon and H. Ockendon, Resonant surface waves, *J. Fluid Mech.* **59**, 397 (1973).
- [7] J. W. Miles, Resonant motion of a spherical pendulum, *Physica D* **11**, 309 (1984).
- [8] J. W. Miles, Resonantly forced surface waves in a circular cylinder, *J. Fluid Mech.* **149**, 15 (1984).
- [9] M. Reclari, M. Dreyer, S. Tissot, D. Obreschkow, F. M. Wurm, and M. Farhat, Surface wave dynamics in orbital shaken cylindrical containers, *Phys. Fluids* **26**, 052104 (2014).
- [10] A. Bongarzone, M. Guido, and F. Gallaire, An amplitude equation modelling the double-crest swirling in orbital-shaken cylindrical containers, *J. Fluid Mech.* **943**, A28 (2022).
- [11] W. Klöckner and J. Büchs, Advances in shaking technologies, *Trends Biotechnol.* **30**, 307 (2012).
- [12] A. Royon-Lebeaud, E. J. Hopfinger, and A. Cartellier, Liquid sloshing and wave breaking in circular and square-base cylindrical containers, *J. Fluid Mech.* **577**, 467 (2007).
- [13] D. J. Tritton, Ordered and chaotic motion of a forced spherical pendulum, *Eur. J. Phys.* **7**, 162 (1986).
- [14] E. N. Lorenz, Deterministic nonperiodic flow, *J. Atmos. Sci.* **20**, 130 (1963).
- [15] O. M. Faltinsen, I. A. Lukovsky, and A. N. Timokha, Resonant sloshing in an upright annular tank, *J. Fluid Mech.* **804**, 608 (2016).
- [16] H. Lamb, *Hydrodynamics* (Cambridge University Press, Cambridge, 1993).
- [17] A. Marcotte, F. Gallaire, and A. Bongarzone, Super-harmonically resonant swirling waves in longitudinally forced circular cylinders, *J. Fluid Mech.* **966**, A41 (2023).
- [18] See Supplemental Material at <http://link.aps.org/supplemental/10.1103/PhysRevFluids.8.084802> for movies showing an example of irregular motion as well as co- and counterswirling dynamics experimentally observed for  $\bar{a}_x = 1.5\text{mm}$  at  $\alpha = 0.25, 0.50, \text{ and } 0.95$ .
- [19] G. B. Whitham, *Linear and Nonlinear Waves* (Wiley-Interscience, New York, 1974).
- [20] A. H. Nayfeh, *Perturbation Methods* (John Wiley & Sons, New York, 2008).
- [21] F. Viola and F. Gallaire, Theoretical framework to analyze the combined effect of surface tension and viscosity on the damping rate of sloshing waves, *Phys. Rev. Fluids* **3**, 094801 (2018).
- [22] A. Bongarzone, F. Viola, and F. Gallaire, Relaxation of capillary-gravity waves due to contact line nonlinearity: A projection method, *Chaos* **31**, 123124 (2021).
- [23] K. O. Friedrichs, *Spectral Theory of Operators in Hilbert Space* (Springer Science & Business Media, Berlin, 2012).
- [24] A. Bongarzone, A. Bertsch, P. Renaud, and F. Gallaire, Impinging planar jets: Hysteretic behaviour and origin of the self-sustained oscillations, *J. Fluid Mech.* **913**, A51 (2021).
- [25] A. Bongarzone, F. Viola, S. Camarri, and F. Gallaire, Subharmonic parametric instability in nearly brimful circular cylinders: A weakly nonlinear analysis, *J. Fluid Mech.* **947**, A24 (2022).
- [26] F. Viola, P.-T. Brun, and F. Gallaire, Capillary hysteresis in sloshing dynamics: A weakly nonlinear analysis, *J. Fluid Mech.* **837**, 788 (2018).
- [27] I. A. Raynovskyy and A. N. Timokha, *Sloshing in Upright Circular Containers: Theory, Analytical Solutions, and Applications* (CRC Press, Boca Raton, 2020).
- [28] I. A. Raynovskyy and A. N. Timokha, Damped steady-state resonant sloshing in a circular base container, *Fluid Dyn. Res.* **50**, 045502 (2018).
- [29] K. M. Case and W. C. Parkinson, Damping of surface waves in an incompressible liquid, *J. Fluid Mech.* **2**, 172 (1957).
- [30] J. W. Miles, Surface-wave damping in closed basins, *Proc. R. Soc. A: Math. Phys. Eng. Sci.* **297**, 459 (1967).



- [31] D. M. Henderson and J. W. Miles, Single-mode faraday waves in small cylinders, *J. Fluid Mech.* **213**, 95 (1990).
- [32] B. Cocciaro, S. Faetti, and C. Festa, Experimental investigation of capillarity effects on surface gravity waves: Non-wetting boundary conditions, *J. Fluid Mech.* **246**, 43 (1993).
- [33] D. M. Henderson and J. W. Miles, Surface-wave damping in a circular cylinder with a fixed contact line, *J. Fluid Mech.* **275**, 285 (1994).
- [34] G. H. Keulegan, Energy dissipation in standing waves in rectangular basins, *J. Fluid Mech.* **6**, 33 (1959).
- [35] E. B. Dussan V, On the spreading of liquids on solid surfaces: Static and dynamic contact lines, *Annu. Rev. Fluid Mech.* **11**, 371 (1979).
- [36] L. M. Hocking, The damping of capillary-gravity waves at a rigid boundary, *J. Fluid Mech.* **179**, 253 (1987).
- [37] B. Dollet, É. Lorenceau, and F. Gallaire, Transition from Exponentially Damped to Finite-Time Arrest Liquid Oscillations Induced by Contact Line Hysteresis, *Phys. Rev. Lett.* **124**, 104502 (2020).
- [38] B. Bäuerlein and K. Avila, Phase lag predicts nonlinear response maxima in liquid-sloshing experiments, *J. Fluid Mech.* **925**, A22 (2021).
- [39] A. Miliaiev and A. Timokha, Viscous damping of steady-state resonant sloshing in a clean rectangular tank, *J. Fluid Mech.* **965**, R1 (2023).
- [40] J. Bouvard, W. Herreman, and F. Moisy, Mean mass transport in an orbitally shaken cylindrical container, *Phys. Rev. Fluids* **2**, 084801 (2017).